Phase-field investigation of rod eutectic morphologies under geometrical confinement

Melis Şerefoğlu, R. E. Napolitano, and Mathis Plapp

Phys. Rev. E **84**, 011614 — Published 29 July 2011

DOI: 10.1103/PhysRevE.84.011614

Phase-field investigation of rod eutectic morphologies under geometrical confinement

Melis Şerefoğlu*† and R. E. Napolitano
Department of Materials Science and Engineering, Iowa State University, Ames, IA, USA

Mathis Plapp
Physique de la Matière Condensée, École Polytechnique, CNRS, 91128 Palaiseau, France

Three-dimensional phase-field simulations are employed to investigate rod-type eutectic growth morphologies in confined geometry. Distinct solutions are found to depend on this confinement effect, with the rod array basis vectors and their included angle (α) changing to accommodate the geometrical constraint. Specific morphologies are observed, including rods of circular cross-section, rods of distorted (elliptical) cross section, rods of "peanut-shaped" cross-section, and lamellar structures. The results show that for a fixed value of $\alpha > 10^\circ$, the usual (hexagonal) arrays of circular rods are stable in a broad range of spacings, with a transition to the peanut-shaped cross sectioned rods occurring at large spacings (above 1.5 times the minimum undercooling spacing, λ_{m}), and the advent of rod eliminations at low spacings. Furthermore, a transition from rod to lamellar structures is observed for $\alpha < 10^\circ$ for the phase fraction of 10.5% used in the present study.

PACS numbers: 64.70.D-, 81.30.Fb, 81.30.-t

I. INTRODUCTION

The potential for substantial gains in the physical and mechanical properties of materials indicates the value of realizing precise control over the various multiphase structures that may arise directly from solidification of an alloy melt. Of these, the periodic phase distributions that evolve during the freezing of alloys exhibiting a melting minimum or *eutectic* point constitute the most important class of multiphase solidification morphologies. In such alloys, the behavior of the relevant phase boundaries, combined with diffusive coupling at the multiphase growth front, may yield a variety of characteristic *eutectic structures*, such as regular rod and lamellar patterns, irregular (faceted-nonfaceted) morphologies, numerous more complex periodic patterns, and aperiodic or chaotic multiphase structures [1–3]. Much of our current understanding of eutectic growth morphologies arises from experimental investigations and analytical models, most notably the Jackson-Hunt (JH) analysis and subsequent modifications [4, 5]. While phase-field modeling has led to substantial advancement in the understanding of single-phase solidification dynamics, the application of these methods to quantitative modeling of eutectic solidification has only become possible in the last few years [6–9]. Given these recent developments in multiphase solidification modeling, it is now possible to systematically probe the morphological dynamics involved with eutectic growth to answer several important outstanding questions which limit our ability to understand, predict, control, and ultimately *create* new growth structures.

One way to influence the formation of solidification microstructures is geometrical confinement. Indeed, numerous experiments are carried out in thin-slab geometry where the distance between specimen walls is comparable to or even smaller than the characteristic spacing of the microstructure. The effect of this confinement on dendritic and cellular microstructures has been extensively studied experimentally and numerically [10–23]. In contrast, little information is available on finite-size effects on eutectic patterns [24–27], especially for rod eutectics [28–30]. We have previously reported [28] on the influence of geometrical confinement on the ordering of a rod-type eutectic array. The degree of confinement can be quantified by the ratio of the sample thickness, δ, to the characteristic spacing between rods, λ. Our investigation, which involved directional solidification of succinonitrile-camphor (SCN-DC) transparent eutectic alloy in thin slab geometries of various thicknesses, revealed two main points. First, there exists a specific velocity at which a transition in array basis vectors is observed in specimens that are thick enough to include several rows of rods (that is, δ/λ between 2 and 10). This transition amounts to a 30° rotation of the rod array, which shifts from alignment of 1st nearest neighbors to alignment of 2nd nearest neighbors with the slide wall. This indicates a decisive influence of the geometrical constraint on the array geometry, despite the relatively large thickness of the sample. Second, significant array distortion is observed with decreasing slide thickness, which ultimately leads to a single-row morphology where δ/λ is on the order of unity. In our analysis of these observations, we assumed that the distortion is completely accommodated by reordering of the array with no change in the phase fractions or the shape of the individual rods, and we used a simple geometrical model to describe the rod arrangement as a function of slide thickness that yields

---

*Melis Şerefoğlu is currently a Postdoctoral Research Associate at the Institut des NanoSciences de Paris, CNRS UMR 7588, Université Pierre-et-Marie-Curie (Paris VI), 4 place Jussieu 75005 Paris, France
†Electronic address: `melis.serefoglu@insp.upmc.fr`

excellent agreement with the experimental observations. For the case of very thin slides, which we examine here, such an assumption does not appear to be reasonable. Indeed, as we shall show below, morphologies in thin specimens vary between the two extreme limits of perfectly circular rods and completely lamellar structures, with several distorted rod geometries in between.

In the work reported here, we employ a three-dimensional phase-field model [6] for regular nonfaceted-nonfaceted (nf-nf) eutectic solidification to probe the influence of geometrical constraint over the full range of confinement ($0° \leq \alpha \leq 90°$) from the bulk case to the limit of very thin samples. Specifically, we use simulations to (i) map out the relevant steady-state morphological domains in terms of eutectic spacing and material (i.e. slide) thickness, (ii) examine transitions in growth morphologies and their relative stability, and (iii) investigate the stability and evolution dynamics associated with the important morphological attractors.

II. METHODS

A. Eutectic solidification

During eutectic solidification, the interface temperature of any growing phase ($i = \alpha, \beta$), is given by the generalized Gibbs-Thomson law,

$$T_i^* = T_E - m_i(C^* - C_E) - \Gamma_i \kappa - \frac{V_n}{\mu_i}, \tag{1}$$

where T_E is the eutectic temperature, m_i is the liquidus slope for phase i in the phase diagram, taken at the eutectic point (with $m_\alpha < 0$ and $m_\beta > 0$), C^* is the composition of the liquid at the interface, C_E is the eutectic composition, Γ_i is the Gibbs-Thomson coefficient for phase i ($\Gamma_i = \gamma_{iL} T_E / L_i$, with γ_{iL} being the surface free energy of the iL-interface, and L_i the latent heat associated with the phase change), κ is the interface curvature (in 3D, $\kappa = 1/R_1 + 1/R_2$, where R_1 and R_2 are the principal radii of curvature), V_n is the normal velocity of the interface, and μ_i is the interface mobility of phase i. Note that we have neglected here any crystallographic effects, so that the surface free energies and interface mobilities are isotropic.

In the material frame, the temperature is given by

$$T(z) = T_E + G(z - Vt), \tag{2}$$

which corresponds to directional solidification in constant temperature gradient, G, with pulling speed, V. With C_α and C_β being the respective solidus compositions at the eutectic temperature, we identify a characteristic composition range as $\Delta C_0 = C_\beta - C_\alpha$ and the corresponding characteristic temperature range for each phase as $\Delta T_0^i = |m_i| \Delta C_0$. The relevant physical length scales are then given by

$$l_T^i = \Delta T_0^i / G, \tag{3a}$$

$$d_i = \Gamma_i / \Delta T_0^i, \tag{3b}$$

$$l_D = D/V, \tag{3c}$$

which are the thermal, capillary, and diffusion lengths, respectively, where D is the solute diffusion coefficient in the liquid.

In terms of the scaled concentration field

$$c = \frac{C - C_E}{C_\beta - C_\alpha}, \tag{4}$$

the sharp-interface formulation of the problem includes the diffusion equation in the liquid,

$$\frac{\partial c}{\partial t} = \nabla \cdot D \nabla c, \tag{5}$$

and the standard mass balance condition at moving interfaces is given by,

$$V_n c_i = -D \hat{n} \cdot \nabla c|_{int}, \tag{6}$$

where c_i are the scaled versions of C_i ($i = \alpha, \beta$), $\hat{n}$ is the local interface unit normal pointing into the liquid, and we have supposed in Eq. (6) that the composition difference between liquid and solid is independent of temperature and equal to its value at the eutectic point. Solving Eq. (1) for C^*, defining $\beta_i = 1/\mu_i \Delta T_0^i$, and combining the result with Eqs. (2), (3a) and (4), we express the composition on the liquid side of the interface as

$$c_i^* = \mp \left(\frac{z}{l_T^i} + d_0^i \kappa + \beta_i V_n \right). \tag{7}$$

Since the surface free energies are isotropic, local equilibrium at the three-phase junctions implies Young's law,

$$\sum_{i \neq j} \gamma_{ij} \hat{t}_{ij} = 0, \tag{8}$$

where γ_{ij} are the $i - j$ surface tensions ($i = \alpha, \beta, L$), and $\hat{t}_{ij}$ are the $i - j$ interface unit tangent vectors, all taken at the trijunction point.

B. Phase-field model

For our simulations, we use the model described in detail in Ref. [6], and we will only give the most important elements here. We use the multi-phase-field formalism [37] and describe the interface geometry with a set of three phase fields, p_α, p_β, and p_L, which represent the local volume fraction of each phase such that

$$p_\alpha + p_\beta + p_L = 1 \tag{9}$$

everywhere. The evolution of these phase field is given by

$$\tau(\mathbf{p}) \frac{\partial p_i}{\partial t} = - \left. \frac{\delta F}{\delta p_i} \right|_{p_\alpha + p_\beta + p_L = 1}, \tag{10}$$

where $\mathbf{p}$ represents the set of the three phase fields, and $\tau(\mathbf{p})$ is the relaxation time of the phase fields. This function of $\mathbf{p}$ is constant and equal to τ_α on the α-liquid interface, and constant and equal to τ_β on the β-liquid interface. The dimensionless free energy functional, F, is given by

$$\begin{aligned} F &= \int_V \sum_{i=\alpha,\beta,L} \left[\frac{W^2}{2} \left| \vec{\nabla} p_i \right|^2 + p_i^2(1-p_i)^2 \right] \\ &\quad + \tilde{\lambda} \sum_{i=\alpha,\beta} g_i(\mathbf{p}) \{ B_i(T) - \mu c_i \}. \end{aligned} \tag{11}$$

In this functional, the second term represents a triple-well potential where each minimum corresponds to a pure phase, and the third term ensures the coupling of the phase field to the thermodynamic driving forces. Here, $B_i(T) = c_i(T - T_E)/(m_i \Delta C)$ represents the undercooling of each solid phase with respect to the liquid, the $g_i(\mathbf{p})$ are functions of all the three phase fields that tilt the triple well potential, and μ is a dimensionless chemical potential,

$$\mu = c - \sum_i c_i p_i. \tag{12}$$

The expressions for the functions g_i as well as the complete equations of motion that result from the evaluation of the functional derivative in Eq. (10) are given in Ref. [6]. The evolution equation for the chemical potential is

$$\begin{aligned} \frac{\partial \mu}{\partial t} &= \vec{\nabla} \cdot \left[D(\mathbf{p}) \vec{\nabla} \mu \right] - \sum_i c_i \frac{\partial p_i}{\partial t} \\ &+ \frac{W}{2\sqrt{2}} \vec{\nabla} \cdot \hat{n}_L \sum_{\alpha,\beta} c_i \frac{\partial p_i}{\partial t} \left(\hat{n}_i \cdot \hat{n}_L \right) \end{aligned} \tag{13}$$

with $D(\mathbf{p}) = D p_L$, which corresponds to the one-sided model (no diffusion in the solid). The last term in Eq. (13) is added to the usual diffusion equation in order to avoid spurious solute trapping, and is a generalization of the antitrapping current for dilute alloys [31].

C. Simulation setup

Even though this model allows for quantitative simulations of a large class of alloy solidification problems, the computational resources required for a three-dimensional simulation of SCN-DC solidification with the same parameters as in the experiments are currently out of reach. Furthermore, we are interested in general questions regarding confinement rather than in a precise reproduction of specific experiments. Therefore, we use parameters that are inspired by the phase diagram of SCN-DC, but make several simplifications which increase the efficiency of the simulations. First, the surface tensions of all three interfaces are assumed to be equal, which yields 120° angles between interfaces at trijunctions. As a consequence, the capillary lengths in the model satisfy the relationship [6]

$$d_\alpha |c_\alpha| = d_\beta |c_\beta|. \tag{14}$$

Second, the liquidus slopes are taken to be of equal magnitude. Furthermore, the temperature gradient is taken much larger than the typical experimental values. This is legitimate since the temperature gradient does not have a decisive influence on eutectic solidification patterns. Finally, the pulling velocity is also chosen to be larger than the one in the experiments. However, as long as the Péclet number, λ/l_D, remains much smaller than unity, the system obeys a scaling law [32] according to which the velocity enters the problem only through the determination of the Jackson-Hunt minimum-undercooling spacing $\lambda_{\rm m}$, which varies as $V^{-1/2}$.

It is known that for a given binary system, the determining parameter for the lamellae to rod transition is the volume fraction of the minority phase [4, 9, 33]. We have chosen the values of the concentrations C_i such as to match the molar fractions of SCN-DC phase diagram (Table 1). This yields a volume fraction of 10.5% of the minority phase at T_E. It should be noted, however, that for the actual SCN-DC system, due to difference in molar volume of the phases, this volume fraction is 18% [28].

The free parameters of the model are the interface thickness, W, and the relaxation times, τ_α and τ_β. An asymptotic analysis in the thin-interface limit [6] gives the following relationships with the relevant physical quantities:

$$d_i = a_1 \frac{W}{\tilde{\lambda} |c_i|} \tag{15a}$$

$$\beta_i = a_1 \left(\frac{\tau_i}{|c_i| \tilde{\lambda} W} - a_2 |c_i| \left(\frac{W}{D} \right) \right), \tag{15b}$$

where $a_1 = 2\sqrt{2}/3$ and $a_2 = 0.7464$.

Accurate results can be expected as long as W is kept about one order of magnitude smaller than the relevant length scales present in the physical system. Since our interest is the small Péclet number regime, thermal and diffusion lengths are much larger than the eutectic spacing, λ, and the smallest relevant length scale is the size of the minority phase. Therefore, for a given velocity, we choose the interface thickness to be 1/10 of the diameter of a rod at the minimum undercooling spacing. For $V = 2.92 \mu m/s$, this value is calculated as $W = 7.07 \times 10^{-4} mm$. The relaxation times, τ_i are then chosen to give vanishing kinetic undercooling at the solid-liquid interfaces. From Eq. (15b), this condition requires that $\tau_i = a_2 \tilde{\lambda} |c_i|^2 W^2/D$, which yields $\tau_\alpha = 2.4 \times 10^{-3} s$ and $\tau_\beta = 3.3 \times 10^{-5} s$ for the simulations presented here. In the following, all lengths will be scaled by W, and all times by $\bar{\tau} = (\tau_\alpha + \tau_\beta)/2$. All dimensionless quantities listed in Table I are scaled in this manner.

TABLE I: Material and Simulation Parameters

Parameter	*Value*
C_α (mol %)	99.15
C_β (mol %)	3.87
C_E (mol %)	13.9
m_α (K/mol%)	-1
m_β (K/mol%)	1
Δx	0.8
$\tilde{D}$	1.178
$\tilde{\lambda}$	4.01
$\tilde{V}$	0.005
l_T^α	940.45
l_T^β	940.45

For all simulations, a rectangular simulation cell is used, in which two quarter-rods are initially located in two diagonal corners, as illustrated in Fig. 1. Reflection boundary conditions (i.e. boundary-normal components of all field gradients are fixed to be zero) are used on all sides. Since the volume fraction is fixed and all simulations are initialized with cylindrical rods, the geometry is completely defined by the lateral dimensions, namely, the thickness, δ, and width, w, of the simulation cell. Alternatively, we also use the cell diagonal $\lambda = \sqrt{w^2 + \delta^2}$ and the array angle $\alpha = \mathrm{atan}(\delta/w)$. The auxiliary parameter d (rod diameter) is also shown in Fig. 1.

The simulation cell can actually represent several extended geometries, as illustrated in Fig. 2. On one hand, a perfectly periodic triangular rod array of infinite size exhibits two sets of orthogonal mirror symmetry planes (on which all gradients vanish by symmetry) that run through the center of each rod, and can therefore be reconstructed by successive reflections of the simulation cell (Fig. 2a). On the other hand, the walls of a thin sample also impose a vanishing solute flux (and thus zero gradient of the solute concentration field) at the boundary. Under the assumption that the solid-liquid and solid-solid interfaces make contact angles of 90° with the glass wall, the reduced simulation cell can thus also represent thin samples of various geometries, as sketched in Fig. 2b, and 2c. While this assumption is certainly not realistic, the true contact angles are unknown, and we have restricted our simulations to this case for simplicity.

Keeping the model parameters fixed, the variation of the simulation domain dimensions enables the examination of various cell geometries. The eutectic front is initially placed within the temperature gradient at a location that corresponds to a temperature below T_E. After a period during which the front position oscillates, it stabilizes at a certain average temperature. Under the constraints imposed by the fixed simulation cell dimensions, the linear thermal field, the constant translation velocity, and the reflective lateral boundaries, the phase fields are permitted to evolve freely, and the system response may involve changes in growth morphology, interface temperature, phase fraction, and the uniformity of these. In every case, we continue the simulation until a time-independent structure is reached, and systematically map out the final morphologies as a function of the geometry.

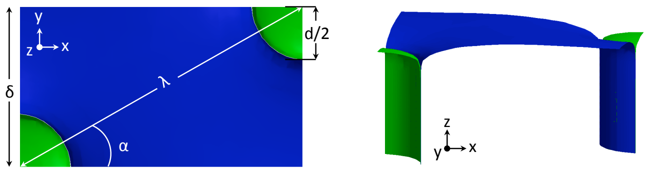

FIG. 1: (Color online) Top and 3D view of the starting simulation cell that contains two quarters of rods located in two diagonal corners. z is the growth direction.

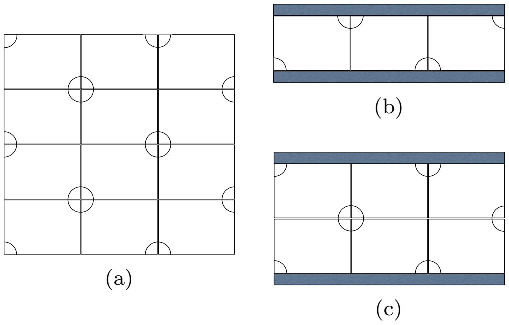
(a)
(b)
(c)

FIG. 2: (Color online) Exploiting the symmetries generated by the reflective boundary conditions in xy plane, several extended geometries can be represented by the simulation cell: a) infinite triangular rod array, b) geometrically-confined array of half rods on the walls, and c) one row of full rods with half rods on the walls.

III. RESULTS

Our overall modeling results are summarized in Fig. 3, where observed morphologies are mapped out in a graph with axes λ and δ/λ. The motivation for this choice is that λ actually represents the initial spacing between rods, whereas δ/λ is related to the aspect ratio of the simulation cell, which determines the distortion of the rod array. Indeed, the points on a given horizontal line of the graph correspond to states with the same angle, α, as shown in the secondary y-axis. Here, only the simulations with α ranging from 0° to 45° are examined for symmetry reasons: due to the fact that we use identical boundary conditions on all sides of the cell, simulations for α and $90° - \alpha$ yield strictly identical results. In Fig. 3, the circles present over the large central portion of the map indicate that the basic triangular array of circular rods is the stable configuration. In this region, the change in δ

is accommodated by distortion of the rod array, observed as a change in the array basis vector angle, α. This is consistent with our previous experimental findings [28].

On the periphery of the map, other morphologies are present. For small values of λ, an instability occurs that leads to the elimination of one of the two rods that are initially present (triangular symbols). In this case, there is a set of corresponding extended geometries, analogous to those in Fig. 2, but with an aligned (rectangular) arrangement. This could represent (a) an infinite rectangular array (R array), (b) a finite set of aligned rods, or (c) a single row of circular rods, located between two walls. It should be noted that the final state actually has only one quarter-rod within the simulation cell. Extended rectangular arrays would most likely be unstable against further rod elimination or rearrangement of rods, similarly to what is observed for rectangular arrays of cellular growth morphologies [22, 23]. At small values of δ/λ which corresponds to values of $\alpha < 10°$, a transition from rods to lamellae takes place, where the pattern becomes effectively one-dimensional. On the border between the rod domain and the lamellar domain, there is a small region where distorted (noncircular) rods are observed. For Fig. 3, rods are defined to be distorted when $|r_x - r_y|/\min(r_x, r_y) > 15\%$, where r_x and r_y are the radii in x and y directions, respectively. Finally, in the upper-right portion of the map, the stable growth morphology consists of severely elongated rods with a peanut-shaped cross section. These remain arranged in a staggered array that could be described as a type of broken-lamellar structure, consistent with the findings of Ref. [9]. In the following, we will examine these steady-state solutions and the transitions between them in more detail.

The steady-state average front undercoolings are plotted in Fig. 4 as a function of λ for rod morphologies at three approximately constant values of α, (15°, 30°, and 45°), indicated by the upper three dotted horizontal lines in Fig. 3. The results for the lamellar structures are also shown.

As shown in Fig. 4, the data can be well described by the Jackson-Hunt theory,

$$\Delta T = K_c \lambda V + \frac{K_r}{\lambda} \tag{16}$$

when the constants K_c and K_r are treated as free parameters. Their values, obtained from fits to the data, are given for each curve. In the JH theory, these constants arise from the averaging of the solutal and curvature undercoolings along the growth front, respectively. It is interesting to note that *both* constants, as well as the ratio between them, vary with α, which indicates that the solute diffusion field, the distribution of curvatures on the interface, and the balance between their effects at the eutectic operating point, are all significantly influenced by the confinement. As a result of these variations, the minimum undercooling spacing, λ_{m}, increases with decreasing α. This indicates that a complete description of

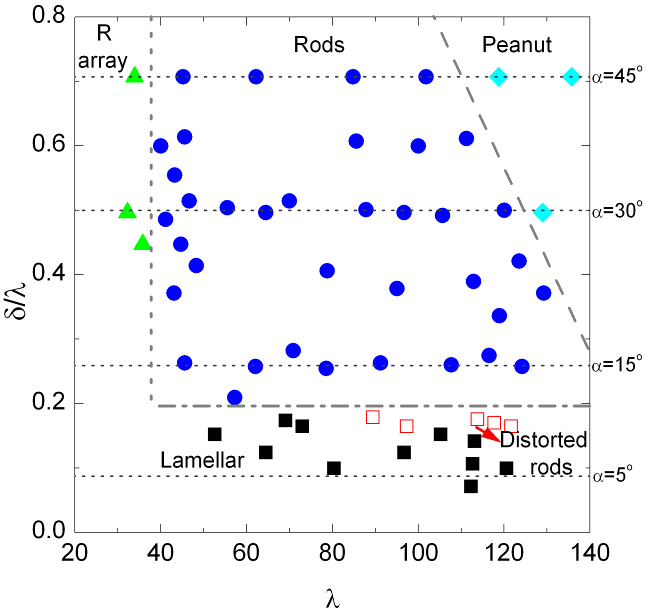

FIG. 3: (Color online) Overall map of the steady-state morphologies, plotted in the $\delta - \lambda - \alpha$ domain of initial simulation conditions.

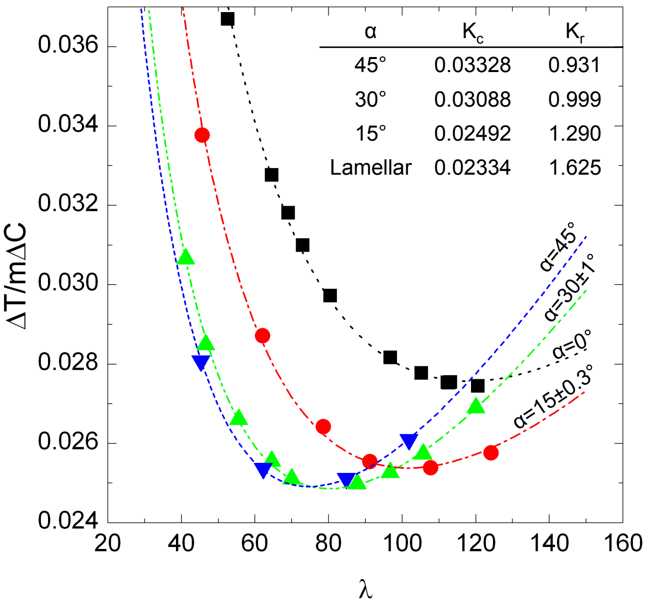

α	K_c	K_r
45°	0.03328	0.931
30°	0.03088	0.999
15°	0.02492	1.290
Lamellar	0.02334	1.625

FIG. 4: (Color online) A summary of simulation results, showing dimensionless undercooling vs. spacing for final steady-state structures of circular rods along the lines $\alpha = 15 \pm 0.3°, 30 \pm 1°, 45°$, as shown in Fig. 3. The simulation results that exhibited lamellar final states are also shown. The JH coefficients for each fitted curve is listed at the upper-right corner, where $\lambda_m^2 V = K_r/K_c$

the system would require the determination of the surface that gives ΔT as a function of λ and α. Furthermore, it can be seen from Fig. 4 that for certain values of λ, the variation of the undercooling with the angle (at a fixed spacing) is non-monotonous, such that there will be a specific α that gives the minimum undercooling for that spacing. Such a correlation implies that, at a constant undercooling, variations in local spacing may be accompanied by corresponding variations in α.

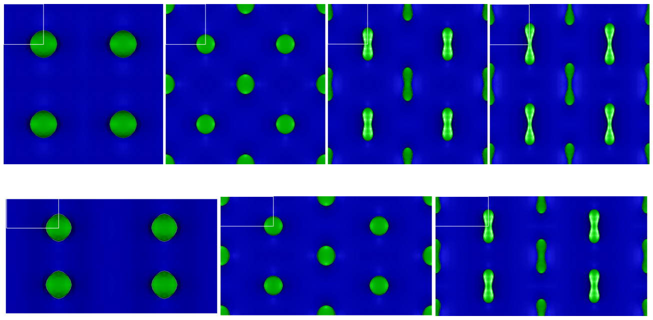

FIG. 5: (Color online) Simulated steady-state structures under the constraint of $\alpha = 45°$ (upper sequence) with λ values of 33.9, 101.8, 118.8, 135.8 and $\alpha = 30 \pm 1°$ (lower sequence) with λ values of 32.2, 96.7, 129.0. These simulations correspond to specific points plotted in Fig.3. The white boxes on the top left corner of the images are the actual simulation cells.

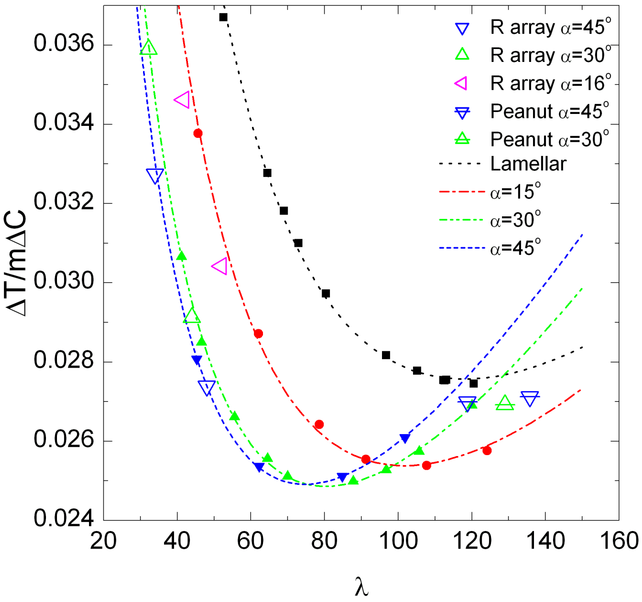

FIG. 6: (Color online) A comparison of other morphologies (empty symbols), including rectangular array of circular rods (R array), and rods with peanut cross-sections (Peanut), with triangular array of circular rods (solid symbols), and lamellae (filled square symbols). The curves are JH fits to circular rods and lamellae data, which are shown in Fig. 4.

We now examine the morphological transitions observed as we sample the map in Fig. 3 along a horizontal line (i.e. keeping α roughly constant). Fig. 5 shows the various morphologies that are found along the $\alpha = 45°$ and $\alpha = 30°$ lines. In both cases, the structure consists of a triangular circular-rod array for intermediate values of λ with transitions to a rectangular array at low λ and a staggered array of peanut-shaped rods at high λ. The transition to the rectangular array corresponds to an elimination of each second vertical (along y) row of rods, which is one of the generic instabilities expected in periodic patterns. The transitions from circular to peanut-shaped rods can be rationalized with the help of the undercooling plots in Fig. 6. Indeed, both for the $\alpha = 45°$ and $\alpha = 30°$, the transition occurs close to the intersection of the respective undercooling curves with the lamellar solution, at approximately $1.6\lambda_{\mathrm{m}}$, also shown in Fig. 6, which suggests that the peanut-shaped structures resembles broken lamellae. The steady-state solution branch always follows the lower of the two curves.

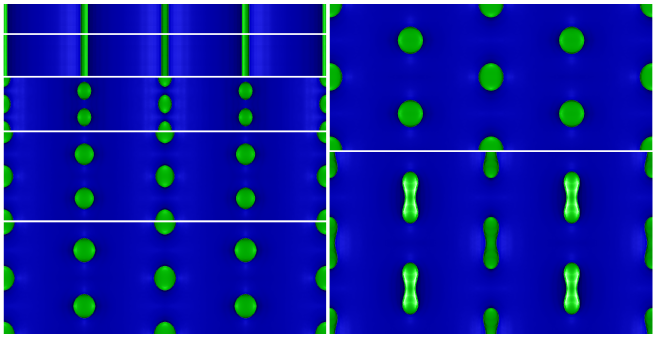

FIG. 7: (Color online) Effect of δ on steady-state microstructures, where the width ($w = 112$) of the simulation cell is kept constant. The starting λ, δ/λ, and α values are (a) 112.64, 0.11, 6.12, (b) 113.14, 0.14, 8.13, (c) 113.77, 0.18, 10.12, (d) 116.48, 0.27, 15.95, (e) 118.93, 0.34, 19.65, (f) 123.48, 0.42, 24.90, (g) 129.00, 0.50, 29.74.

Next, we look more directly at the effect of specimen thickness, δ, on the selected eutectic morphology. The morphological transitions indicated in Fig. 3 are shown in more detail in Fig. 7 for a constant width, w, revealing the rod to lamellae (3D-2D) transition for thin slides and the transition to peanut-shaped rods for large thicknesses. Fig. 3 shows that the rod structure gives way to a lamellar structure for $\delta/\lambda < 0.2$, which corresponds to an α value of approximately 10°.

An important question is whether the observed morphologies are dependent on the choice of the initial and boundary conditions. Here, we have limited ourselves to simulations carried out in the reduced simulation cell shown in Fig. 1 that contains only two quarters of rods. However, simulations carried out with the same model in Ref. [9] with larger cells containing several rods (which, thus, were not submitted to the same boundary conditions) did not yield any other steady-state morphologies.

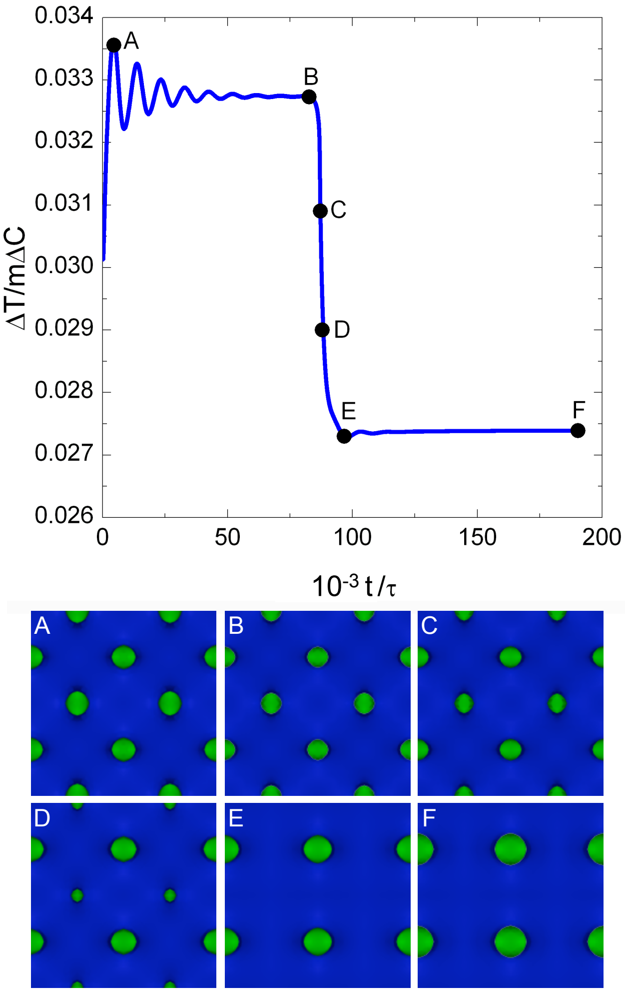

FIG. 8: (Color online) Evolution dynamics for the triangular to rectangular rod array transition for $\alpha = 45°$, where the rectangular rod array emerges after some transient time. The sequence of structures shows that the decease in undercooling is associated with an increase in spacing that arises from the disappearance of alternating rods.

Therefore, we believe that we have correctly captured the dependence of the final morphology on the initial position of the rods which is controlled by the cell geometry. It was also shown in Ref. [9] that for rods with higher volume fraction than the one used here, two distinct final states could be reached for the same parameters and simulation box geometry by starting from two different initial conditions. No such phenomenon is observed in the present study.

Representative evolution dynamics for the triangular to rectangular array transition are shown in Fig. 8, which shows both the undercooling and the corresponding morphologies as a function of time. As can be seen in Fig. 8, the undercooling curve reaches a plateau at point “B”, where the morphology is still the original staggered array, just before the rapid transition to the final rectangular array takes place. This indicates that the staggered array is still a fixed point for the dynamics of the system, but that this fixed point has become unstable. The undercooling corresponding to this plateau, when plotted in the ΔT versus λ plot, falls right on the corresponding JH curves for $\alpha = 30°$ and $\alpha = 45°$ (the empty triangles at higher ΔT values in Fig. 6). Quite surprisingly, the undercoolings for the final steady-state morphology also falls on the same curves when the characteristic spacing is calculated as the mean value of horizontal and vertical spacings in the rectangular array ($\lambda = \delta + w$), although the structure has changed from a triangular to a rectangular array. This indicates that the determining parameter for the JH curves is the aspect ratio of the simulation cell which remains, of course, unchanged during the morphological transition.

Finally, for a particular simulation with a starting value of $\alpha = 16°$, we have observed two successive transitions, first from a triangular to a rectangular array (the corresponding values of the undercooling are shown as triagles pointing to the left in Fig. 6), and then to lamellae. This indicates that, for a given phase fraction, the transition from rods to lamellae occurs at larger values of α for rectangular arrays, which is quite intuitive since the diameter of the rods is larger in that state. More precisely, the occurrence of the rods to lamellae transition depends on the ratio of d to δ.

The evolution from circular to peanut-shaped rods is illustrated in Fig. 9, which shows the undercooling as a function of time along with the corresponding morphologies. The rods are initially circular (point “A”), but with time they become elongated (point “B”), and finally evolve to the peanut-shaped cross-sectioned structure (point “C”) which persists as the stable steady-state structure. Note that the undercooling of the final structure is lower than the one of mildly elongated rods, despite the large curvatures at the “tips” of the “peanuts”.

IV. SUMMARY AND PERSPECTIVES

We have reported here on a phase-field study of eutectic growth, where simulations are employed to investigate rod-type growth morphologies in constrained geometry. We have characterized various steady-state patterns and the conditions under which they can form, and examined the dynamics of the transitions between them. Our most important findings can be summarized as follows.

1. Confinement can trigger a transition from rods to lamellae, even for growth conditions and alloy compositions where rods would be the preferred morphology in extended systems.

2. A stability map of different morphologies involving rods of circular cross section with triangular and rectangular arrays, rods of peanut-shaped cross section, and lamellae is obtained. At low spacings, a rod elimination instability occurs that transforms

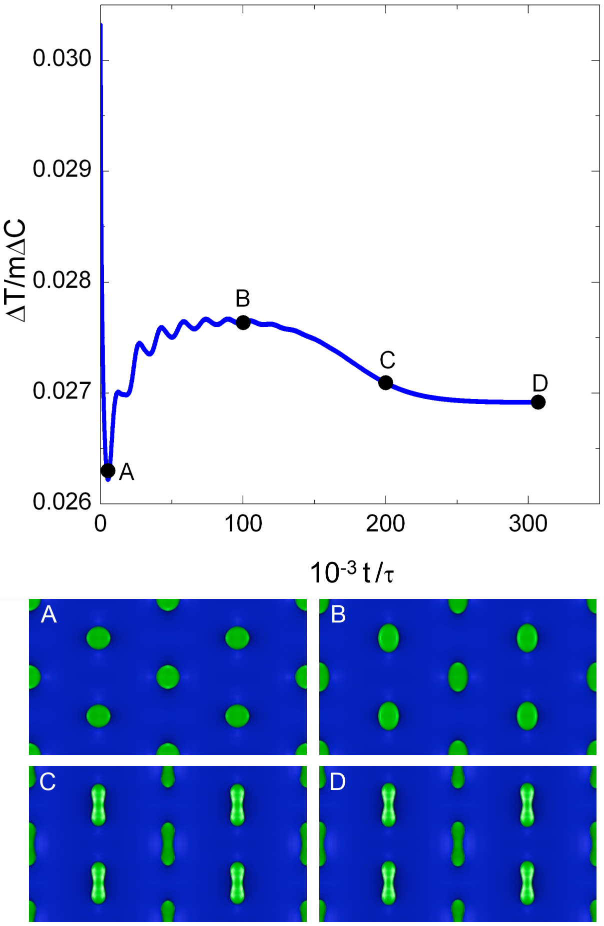

FIG. 9: (Color online) Evolution dynamics of rod to peanut transition with the corresponding morphologies.

the original triangular rod array into a rectangular one. A shape transition to peanut-shaped cross-sectioned rods occurs for larger values of spacing, as already observed in Ref. [9].

3. The undercooling of steady-state rod arrays can be well described by a fit to a Jackson-Hunt law, with coefficients that depend on the array distortion (expressed by the angle between array basis vectors). Both triangular and rectangular arrays can be described by the same curve if the rod spacings are properly defined.

It is clear that phase-field simulations are a valuable tool to investigate the influence of confinement. We have performed simulations here for a fixed set of material parameters and various geometries. It would be interesting to explore the influence of the materials parameters (such as volume fractions of the solid phases, ratio of the liquidus slopes, and ratio of the surface tensions) on the observed transitions. However, a large number of simulations would be required to get a reasonably complete picture, which remains a computational challenge.

A particularly interesting question that will be addressed in a future work is the influence of the wetting properties on the confined states. The precise value of the sample thickness where the transition occurs will certainly depend on the wetting properties of the sample walls. Qualitatively, this phenomenon should be robust and therefore observable in experiments. The measurement of contact angles is delicate if not impossible in experiments. In phase-field simulations, however, arbitrary contact angles can be implemented by simple changes in the boundary conditions (see for example Ref. [43]). Therefore, such simulations offer a unique opportunity for investigating this issue.

Acknowledgments

This work was supported by the National Science Foundation (NSF), Division of Materials Research, under Award No. 0237566. MP acknowledges financial support from Centre National d'Etudes Spatiales (France).

---

[1] M. Asta, C. Beckermann, A. Karma, W. Kurz, R. Napolitano, M. Plapp, G. Purdy, M. Rappaz, and R. Trivedi, Acta Mater. **57**, 941 (2009).
[2] W. J. Boettinger, S. R. Coriell, A. L. Greer, A. Karma, W. Kurz, M. Rappaz, and R. Trivedi, Acta Mater. **48**, 43 (2000).
[3] M. Ginibre, S. Akamatsu, and G. Faivre, Phys. Rev. E **56**, 780 (1997).
[4] K. A. Jackson and J. D. Hunt, Trans. Metall. Soc. AIME **236**, 1129 (1966).
[5] R. Trivedi, P. Magnin, and W. Kurz, Acta Metall. **35**, 971 (1987).
[6] R. Folch and M. Plapp, Phys. Rev. E **72**, 011602 (2005).
[7] A. Parisi and M. Plapp, Acta Mater. **56**, 1348 (2008).
[8] M. Perrut, A. Parisi, S. Akamatsu, S. Bottin-Rousseau, G. Faivre, and M. Plapp, Acta Mater. **58**, 1761 (2010).
[9] A. Parisi and M. Plapp, EPL **90**, 26010 (2010).
[10] J. H. Jeong, N. Goldenfeld, J. A. Dantzig, Phys. Rev. E, **64** 041602, (2001).
[11] B. P. Athreya, J. A. Dantzig, S. Liu, R. Trivedi, Philosophical Magazine **86**, 3739-56 (2006).
[12] L. M. Fabietti, J. A. Sekhar, Journal of Materials Science **29**, 473-7 (1994).
[13] L. M. Fabietti, J. A. Sekhar, Metallurgical Transactions A **23**, 3361-8 (1992).
[14] A. Semoroz, S. Henry, M. Rappaz, Metallurgical and Materials Transactions A **31**, 487-95 (2000).
[15] R. Trivedi, H. Miyahara, P. Mazumder, E. Simsek, S. N.Tewari, Journal of Crystal Growth **222**, 365-79 (2001).

[16] J. D. Hunt, S. Z Lu, Materials Science and Engineering A **173**, 79-83 (1993).

[17] S. Z. Lu, J. D. Hunt, Journal of Crystal Growth **123**, 17-34 (1992).

[18] L. X. Liu, J. S. Kirkaldy, Journal of Crystal Growth **140**, 115-22 (1994).

[19] J. A. Sekhar, R. Trivedi, Materials Science and Engineering A **114**, 133-46 (1989).

[20] D. Shangguan, J. D. Hunt, Metallurgical Transactions A **22**, 1683-7 (1991).

[21] N. F. Dean, A. Mortensen, M. C. Flemings, Metallurgical and Materials Transactions A **26**, 2141-53 (1995).

[22] M. Plapp and M. Dejmek, Europhys. Lett. **65**, 276 (2004).

[23] S. Gurevich, A. Karma, M. Plapp, and R. Trivedi, Phys. Rev. E **81**, 011603 (2010).

[24] V. Seetharaman, R. Trivedi, Metallurgical Transactions **19A**, 2955 (1988).

[25] V. Seetharaman, R. Trivedi, in Solidification processing of eutectic alloys The Metallurgical Society, Warrendale, Pennsylvania, D.M. Stefanescu, G.J. Abbaschian, R.J. Bayuzik (Editors), 65-85 (1988).

[26] R. Trivedi, J. T. Mason, J. D. Verhoeven, W. Kurz, Metallurgical Transactions A **22A**, 2523-33 (1991).

[27] S. Akamatsu, S. Bottin-Rousseau, G. Faivre, Philosophical Magazine **86**, 3703-15 (2006).

[28] M. Şerefoğlu and R. E. Napolitano, Acta Mater. **56**, 3862 (2008).

[29] M. Şerefoğlu, and R.E. Napolitano, International Journal of Cast Metal Research **22**, 1-4 (2009).

[30] M. Şerefoğlu, and R.E. Napolitano, Acta Mater. **59**, 1048-57 (2011).

[31] B. Echebarria, R. Folch, A. Karma, and M. Plapp, Phys. Rev. E. **70**, 061604 (2004).

[32] K. Kassner, C. Misbah, Phys. Rev. Lett. **66**, 445 (1991).

[33] F. R. Mollard, M. C. Flemings, Trans. Met. Soc. AIME **239**, 1534 (1967).

[34] A. Karma and M. Plapp, JOM **56**, 28 (2004).

[35] S. Akamatsu, M. Plapp, G. Faivre, and A. Karma, Phys. Rev. E **66**, 030501 (2002).

[36] A. Karma, Phys. Rev. Lett. **87**, 115701 (2001).

[37] I. Steinbach, F. Pezzolla, B. Nestler, M. Seeßelberg, R. Prieler, G. J. Schmitz, and J. L. L. Rezende, Physica D **94**, 135 (1996).

[38] J. Tiaden, B. Nestler, H.-J. Diepers, and I. Steinbach, Physica D **115**, 73 (1998).

[39] A. Karma and W.-J. Rappel, Phys. Rev. E **53**, R3017 (1996).

[40] A. Karma and W.-J. Rappel, Phys. Rev. E **57**, 4323 (1998).

[41] V. T. Witusiewicz, L. Sturz, U. Hecht, and S. Rex, Acta Mater. **52**, 4561 (2004).

[42] S. Akamatsu, S. Bottin-Rousseau, M. Perrut, G. Faivre, V. T. Witusiewicz, and L. Sturz, J. Cryst. Growth **299**, 418 (2007).

[43] L. Gránásy, T. Pusztai, D. Saylor, and J. A. Warren, Phys. Rev. Lett. **98**, 035703 (2007).